

RESEARCH ARTICLE

10.1002/2015JB011892

Key Points:

- Correcting for shear wave splitting yields high-precision tremor locations
- Many migration patterns are controlled by the orientation of the main front
- Some rapid tremor reversals start by propagating along the main front

Supporting Information:

- Figures S1–S16
- Text S1
- Text S2
- Text S3
- Text S4
- Text S5
- Text S6

Correspondence to:

Y. Peng,
yajun@princeton.edu

Citation:

Peng, Y., A. M. Rubin, M. G. Bostock, and J. G. Armbruster (2015), High-resolution imaging of rapid tremor migrations beneath southern Vancouver Island using cross-station cross correlations, *J. Geophys. Res. Solid Earth*, 120, 4317–4332, doi:10.1002/2015JB011892.

Received 15 JAN 2015

Accepted 21 APR 2015

Accepted article online 24 APR 2015

Published online 19 JUN 2015

High-resolution imaging of rapid tremor migrations beneath southern Vancouver Island using cross-station cross correlations

Yajun Peng¹, Allan M. Rubin¹, Michael G. Bostock², and John G. Armbruster³

¹Department of Geosciences, Princeton University, Princeton, New Jersey, USA, ²Department of Earth, Ocean and Atmospheric Sciences, The University of British Columbia, Vancouver, British Columbia, Canada, ³Lamont-Doherty Earth Observatory, Columbia University, Palisades, New York, USA

Abstract We develop a cross-station method to detect and locate tremor and low-frequency earthquakes (LFEs), based on the original work of Armbruster et al. (2014) that compares waveforms from the same time window at stations separated by roughly 10 km. To improve the signal-to-noise ratio, we first rotate the horizontal components into the empirical shear wave particle motion direction. The large-scale “rapid tremor reversals” beneath southern Vancouver Island are best recorded by stations that exhibit pronounced shear wave splitting, which obscures this optimal direction. We correct for splitting using the stacked templates of 11 low-frequency earthquake families obtained in this region by Bostock et al. (2012). We find that the style of rapid tremor migrations (RTMs) evolves as the main front passes over a region. Very close to the main front, numerous small-scale migrations occur with recurrence intervals far shorter than tidal periods. These usually propagate along the main front even when that is not parallel to dip. Several larger RTMs propagating along the main front have prominent elongation orthogonal to the propagation direction, inconsistent with the interpretation that their large propagation speed is an “apparent” velocity caused by the slow main front intersecting a preexisting linear structure on the plate interface. Farther behind the main front, RTMs gradually progress to being tidally modulated and have generally slower propagation speeds. Many reversal-like RTMs are observed, some of which evolve from fronts initially propagating along the main front. These reversals are sometimes coherent across regions of low tremor density.

1. Introduction

Episodic tremor and slip (ETS) [Rogers and Dragert, 2003; Obara et al., 2004] represents an important component of the subduction zone seismic cycle, typically occurring on the plate interface downdip of the locked portion of faults capable of producing earthquakes up to magnitude 9 [Beroza and Ide, 2011]. Macroscopic properties of ETS, such as the total displacement accumulated during each episode, can be constrained by geodetic observations [Szeliga et al., 2008; Wech et al., 2009; Dragert and Wang, 2011]; however, the spatiotemporal resolution of such data sets is low. On the other hand, remarkable spatial and temporal correlation between slow slip and tremor has been reported in Cascadia and Japan [Rogers and Dragert, 2003; Obara et al., 2004; Bartlow et al., 2011; Dragert and Wang, 2011; Hawthorne and Rubin, 2013]. Additionally, a large portion of tremor can be explained by low-frequency earthquake (LFE) swarms [Shelly et al., 2007a], with locations and focal mechanisms consistent with shear slip on the plate interface [Shelly et al., 2007a; Ide et al., 2007; Royer and Bostock, 2013]. Thus, tremor is generally interpreted as the seismic manifestation of slow slip and has been used extensively to infer the detailed temporal and spatial history of slow slip [e.g., Shelly et al., 2007b; Ghosh et al., 2010; Houston et al., 2011; Obara, 2012; Rubin and Armbruster, 2013]. Several modes of tremor migrations have been reported: While the main tremor front propagates along strike at speeds of 5–15 km/d [e.g., Wech et al., 2009; Kao et al., 2009; Ito et al., 2007], short-term tremor migrations behind the main front, propagating either roughly along dip [Shelly et al., 2007b; Ghosh et al., 2010] or back in the direction from which the main front came [Houston et al., 2011; Obara, 2012; Rubin and Armbruster, 2013], move tens to hundreds of times faster. Here we assume the main slow slip front to be coincident in space and time with the leading edge of the slowly migrating tremor front.

In this study, we apply a new high-resolution method to locate LFEs beneath southern Vancouver Island, by taking advantage of coherence in seismic waves of tremor among stations separated by roughly 10 km

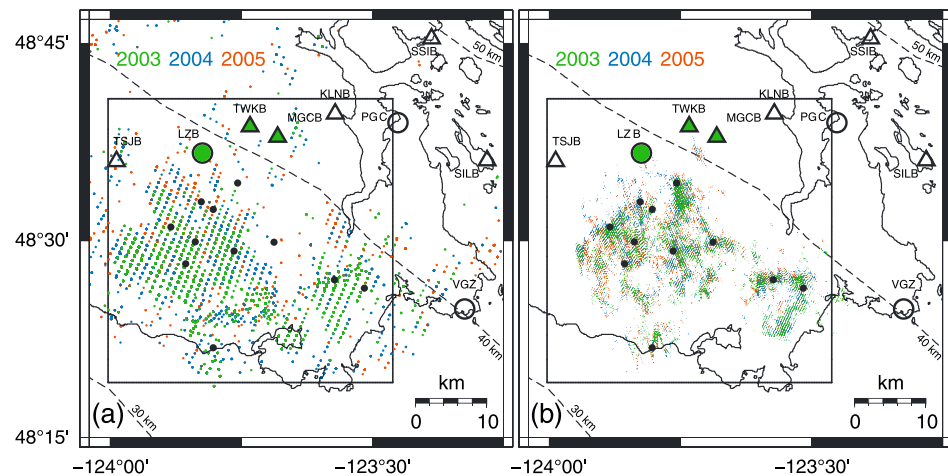


Figure 1. (a) Long-window tremor locations using stations LZB-TWKB-MGCB, from *Armbruster and Kim* [2010], during the major slow slip episodes in March 2003 (green dots), July 2004 (blue), and September 2005 (red) beneath southern Vancouver Island (green on top of blue on top of red). Triangles are POLARIS stations and large circles are part of the CNSN permanent network. LZB, TWKB, and MGCB are colored green. The solid rectangle outlines the study region shown in Figures 4 and 6–10. Black circles are 11 cross-time templates from *Bostock et al.* [2012] selected to correct for shear wave splitting. They are located here by using cross correlation to measure the relative arrival times at the three stations, and then using Hypoinverse [*Klein*, 2002] while forcing the template to lie on the plate interface of *McCrary et al.* [2004] (depth contours shown by dashed lines). (b) Tremor locations using long time windows, after correcting for shear wave splitting using the LZB-TWKB-MGCB trio during 1–8 March 2003, 12–21 July 2004, and 11–18 September 2005. Detections >8 km away from their parent templates are not included. Symbols are as in Figure 1a. Grid spacing is finer in Figure 1b than in Figure 1a because the time offsets for the latter have been interpolated to 0.25 samples.

[*Rubin and Armbruster*, 2013; *Armbruster et al.*, 2014]. We refer to this approach as “cross station”, as opposed to the “cross-time” method that compares the waveforms of a target LFE with either a nearby preidentified LFE [*Shelly et al.*, 2007a], or a stack of many nearly colocated LFEs [*Brown et al.*, 2009; *Shelly*, 2010; *Bostock et al.*, 2012]. *Armbruster et al.* [2014] correlated overlapping long (150 s) time windows at three stations, PGC-SSIB-SILB (Figure 1), which are separated by 10–20 km. They found empirically that the signal-to-noise ratio was improved by rotating the horizontal seismograms into the “optimal” direction, that being the direction which maximized the maximum cross-correlation coefficient (CC_{max}) between stations; they interpreted this as the shear wave polarization direction. For all successful detections they performed a 5-D grid search (the rotation angle at each of the three stations plus the two independent time offsets) to maximize the sum of the 3 CC_{max} values (one for each station pair). *Rubin and Armbruster* [2013] emphasized short (4 s) windows by adopting the optimal station rotations determined by *Armbruster et al.* [2014] for particular subregions of their study area, given that the optimal directions varied smoothly in space for their adopted trio of stations.

Although it appears to give very accurate tremor locations, a shortcoming of the cross-station method is that a given three-station detector is sensitive to only portions of a fault surface. Stations too close to a shear wave node or far enough from the source to generate *P*-to-*S* conversions at the surface are not expected to correlate well with one another. This effect can be seen in Figure S1 in the supporting information, where we compare tremor locations for long-window detections using the trios LZB-TWKB-MGCB [*Armbruster and Kim*, 2010] and PGC-SSIB-SILB [*Armbruster et al.*, 2014]. For a gently dipping thrust fault, the shear wave radiation is strongest at stations above a spot slightly downdip of the source region; although there is some overlapping of the images in Figure S1, this is why the LZB trio sees sources generally updip of those seen by the PGC trio. We note that in order to locate tremor events relying on only three stations, the assumption that the tremor occurs on the plate interface must be introduced. This location method likely results in a systematic shift of a few kilometers between the absolute locations determined by different station trios. However, the relative locations, which are more relevant to imaging tremor migrations, are expected to be relatively well preserved in the catalog derived from a single trio. This is supported by the fact that where the two catalogs overlap in Figure S1, the same migrations seen by the two trios show consistent patterns (Figure S2).

In this study we focus on the LZB trio instead of the PGC trio used by *Armbruster et al.* [2014] and *Rubin and Armbruster* [2013]. The LZB trio is well-positioned to image the region of rapid tremor reversals (RTRs)

observed by *Houston et al.* [2011], that generally occur in the updip portion of the ETS source region. These reversals cover a much larger area of the fault than the roughly 10 km region examined in detail by *Rubin and Armbruster* [2013]. Furthermore, the tremor source regions in this updip region seem to be less isolated than those well imaged by the PGC trio (Figure S1). This might allow us to use tremor migrations in this updip region to characterize more fully the form of the underlying slow slip fronts.

However, in contrast to our experience with the PGC stations, we have noticed that the optimal directions for the LZB stations independently determined for each detection sometimes vary abruptly on very short spatial scales across the study region. This observation suggests that the pronounced shear wave splitting beneath those stations [*Bostock and Christensen*, 2012] might obscure the real shear wave polarization directions, which would potentially lower the signal-to-noise ratio and hence the detecting ability and location accuracy of a cross-station detector. To account for splitting using a direct extension of the method of *Armbruster et al.* [2014] would require a 7-D search for each station pair (two fast directions and split delay times, two optimal directions, and the time offset between the two stations). This is computationally impractical and does not necessarily guarantee a physical solution. Instead, we obtain empirical shear wave polarization angles after correcting for shear wave splitting using cross-time LFE templates from *Bostock et al.* [2012]. In other words, we determine the splitting parameters and apparent shear wave polarization direction independently at each station, rather than by maximizing the cross-correlation coefficient between pairs of stations. In section 2, we compare the split-corrected cross-station locations with the uncorrected. In section 3, we present fine-scale migration patterns of rapid tremor migrations (RTMs) and discuss the implications for slow slip fronts.

2. Data and Methodology

In this study we use horizontal components at stations from the Canadian National Seismograph Network (CNSN) and temporary POLARIS deployment. The POLARIS stations, in place from 2003 to 2006, are downsampled from 100 to 40 s.p.s., the same as the sampling frequency of the permanent stations, and the data are filtered from 1.5 to 6 Hz to emphasize frequencies with good signal-to-noise ratio [*Rubin and Armbruster*, 2013].

2.1. Shear Wave Splitting Corrections

Assuming the splitting to be dominated by one layer of anisotropy [*Matharu et al.*, 2014], we perform a grid search of split times and fast polarization directions to maximize the CC_{\max} between the fast and slow components of the cross-time templates at each station [*Fukao*, 1984; *Bowman and Ando*, 1987]. To avoid subjectivity of window selection, we use 100 moving windows with lengths from 1 to 1.45 s containing the main arrival and find a stable split solution [*Teanby et al.*, 2004]. The CC_{\max} values between the fast and slow components are usually greater than 0.9. One example of shear wave splitting for a cross-time template is shown in Figure 2 for stations TWKB and LZB. We double check the results using standard splitting analysis by minimizing the smaller eigenvalue of the split-corrected covariance matrix of four dot products from the fast and slow components [*Silver and Chan*, 1991]. We accept the solution only if the split time is ≥ 2 samples (0.05 s). The fast polarization directions at LZB, TWKB, and MGCB (Figure S3) are consistent with the measurements of *Bostock and Christensen* [2012]. The split times for different source-station geometries show a smoothly varying spatial dependence, ranging from two to nine samples, presumably caused by differences in raypaths.

By time shifting the fast component to align with the slow component, we obtain corrected waveforms for the templates and construct a covariance matrix from the east and north components to solve for the eigenvector corresponding to the maximum eigenvalue, which indicates the (corrected) empirical shear wave polarization direction. For the example in Figure 2, the CC_{\max} between the two optimal components at TWKB and LZB increases from 0.659 to 0.844 after the splitting correction. The CC_{\max} values for most templates are not improved as dramatically, possibly because the three stations are close enough to one another that the splitting corrections are similar, making the uncorrected optimal components for the templates reasonably similar to one another. However, as is shown in Figures 2c and 2d, the energy of the orthogonal components is almost completely transferred to the optimal components after the splitting correction. The amplified energy of the optimal components leads to enhanced signal-to-noise ratio when locating tremor. In addition, we show in section 2.3 that after the splitting correction the ratio of the energy of the optimal component to that of the orthogonal is a powerful quality control measure to weed out false detections. We find that the corrected polarization directions for the cross-time templates align better with the expected slip vector on the fault (Figure S4), consistent with previous polarization analysis of tremor from other regions in Cascadia

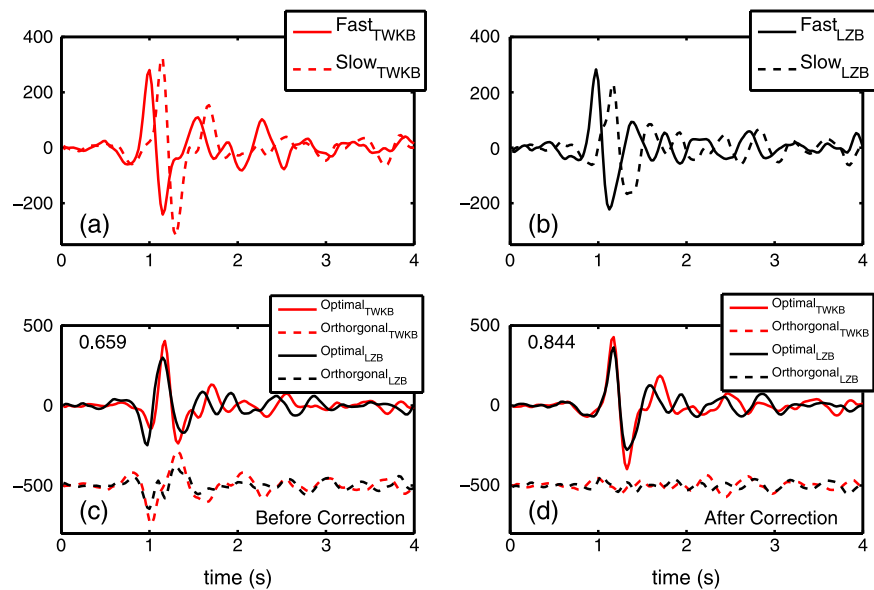


Figure 2. Waveforms of one of the 11 stacked LFE templates from *Bostock et al.* [2012] used in this study. (a, b): Waveforms rotated into the fast (solid lines) and slow (dashed lines) directions for stations TWKB and LZB, respectively. Amplitude scale is arbitrary. (c) Aligned optimal components (solid lines) and orthogonal components (dashed lines) at TWKB (red) and LZB (black), obtained by the same method described in section 2.1, but without splitting corrections. The CC_{max} of the two optimal components is 0.659. The orthogonal components are moved downward for comparison. (d) Aligned optimal components and orthogonal components at TWKB (red) and LZB (black) after splitting corrections. The CC_{max} of the two optimal components has increased to 0.844.

[*Wech and Creager, 2007; Royer and Bostock, 2013; Armbruster et al., 2014; Matharu et al., 2014*], and with the expectation from focal mechanisms of LFEs in Japan [*Ide et al., 2007*].

2.2. Long-Window Detections

We focus on time periods during the major ETS episodes captured by the POLARIS deployment: 11–18 September 2005, 12–21 July 2004, and 1–8 March 2003 [*Nicholson et al., 2005*]. The corrected empirical polarization directions and time offsets of the templates are adopted to image limited source regions centered on the corresponding templates. We first use 128 s windows with a lag of 8 s, which gives 10,800 observations per day. We shift the station time offsets for LZB and MGCB relative to TWKB by up to ± 14 samples and interpolate the cross-correlation functions assuming a parabolic form near the maximum CC for each station pair. Not all of the LFE families, and hence the templates, are mutually independent since many of them seem to share a significant number of detections. So for computational efficiency we select only 11 templates (Figure 1) for which we can get robust splitting corrections. For a successful detection the thresholds for the average CC_{max} is set to be 0.2. The summation of the circuit of time offsets (Sum_{off}) is required to be less than 1.5 samples (at 40 Hz) [*Rubin and Armbruster, 2013*]. These CC_{max} and Sum_{off} thresholds are set by trial and error. In principle, the cutoff should be high enough to weed out most presumed false detections that are not spatially and temporally clustered, without reducing too significantly the number of detections that are spatially and temporally clustered. Given a successful detection, we then interpolate the cross-correlation functions for the three station pairs to 0.25 samples and choose the time offsets that maximize the average CC_{max} while simultaneously forcing Sum_{off} to be 0. To remain a successful detection, this CC_{max} is again required to be ≥ 0.2 .

We next merge the 11 catalogs of “daughter” detections corresponding to each template. Since for one time window the selection criteria might be met using different splitting corrections and polarization angles from the different templates, we retain only the detection with the highest average CC_{max} value. As in *Armbruster et al.* [2014], locations are determined iteratively using Hypoinverse [*Klein, 2002*] and the 1-D velocity model of the Pacific Northwest Seismic Network (Puget Sound P3) [*Crosson, 1976*], while forcing the tremor to be located on the plate interface as modeled by *McCrory et al.* [2004]. As expected, this assumption, plus the reliance on three stations rather than the many used by *Bostock et al.* [2012], leads to shifts in space for the templates relative to the locations of *Bostock et al.* [2012]. However, the relative locations of the templates are

preserved reasonably well. Following *Bostock et al.* [2012] and *Arnbruster et al.* [2014], we do not apply static station corrections to the arrival times, since we expect them to exert little influence on the relative locations.

Only detections within 8 km of their parent template are included in the catalog. The spatially varying splitting corrections could increase the relative location error of nearby events, if they are tied to different templates. We estimate the magnitude of this effect in section 3.1. Figure 1b shows the long-window detections using the split-corrected empirical polarization angles. Note that the southernmost portion of the study region may be highly undersampled since we use only one template in this area that is far from the others. In addition, the irregular grid spacing for tremor locations in this region is very likely to be not physical and to result from the imperfect 1-D velocity model employed. However, the rest of the study region, generally closer to the LZB stations, does not appear to suffer from this problem. In comparison to the original locations of *Arnbruster and Kim* [2010] (Figure 1a), the spatial patterns of our corrected tremor locations are much more localized, suggesting significantly increased location accuracy. The overlapping of tremor source regions during the three ETS events shows high reproducibility.

2.3. Short-Window Detections

Rubin and Arnbruster [2013] showed that long-window locations tend to be averages of the contemporaneous short-window locations, with the latter showing more detailed structure. Therefore, for the rest of this paper we locate tremor using 4 s windows with a lag of 1 s to image detailed tremor migration patterns. The threshold for the average CC_{\max} of the three station pairs for the shorter windows, again chosen empirically, is set to be 0.4, and Sum_{off} remains at 1.5 samples. The same procedure for the long-window detections is applied, with the exception that to avoid double counting the same event given overlapping windows, we adopt a two-step approach to removing duplicate detections:

First, we determine the main arrival time for the daughter detections in each of the 11 catalogs by multiplying pairs of optimal components and averaging the three pairs [*Rubin and Arnbruster*, 2013]:

$$\dot{E}(t) = \frac{S_{1\text{op}}(t)S_{2\text{op}}(t'_2) + S_{1\text{op}}(t)S_{3\text{op}}(t'_3) + S_{2\text{op}}(t'_2)S_{3\text{op}}(t'_3)}{3}. \quad (1)$$

Here $\dot{E}(t)$ denotes a proxy for the coherent radiated energy rate in the adopted passband 1.5–6 Hz. The subscript 1, 2, or 3 denotes the station and “op” the optimal component. $S(t)$ is the seismogram and t' accounts for the time offset between station 2 or 3 and the reference station 1 (TWKB). We then save the time of the maximum $\dot{E}(t)$ within each 4 s window. If the most energetic arrivals of multiple windows are separated by < 0.5 s, we retain only the detection with highest CC_{\max} value averaged over the three station pairs.

Second, we introduce the ratio of the energy of the optimal component to that of the orthogonal ($R_{o/o}$) as an additional quality control measure to weed out “false positives.” This is a proxy for signal-to-noise ratio. We find the 1 s interval over which the integral of equation (1) is maximized. Over this interval, we compute $R_{o/o}$ as follows:

$$R_{o/o} = \frac{\sum_{1s} (S_{1\text{op}}^2(t) + S_{2\text{op}}^2(t'_2) + S_{3\text{op}}^2(t'_3))}{\sum_{1s} (S_{1\text{or}}^2(t) + S_{2\text{or}}^2(t'_2) + S_{3\text{or}}^2(t'_3))}, \quad (2)$$

where the subscript “or” indicates the orthogonal component. $R_{o/o}$ is always positive. We then merge the 11 catalogs, after removing detections with $R_{o/o}$ lower than the threshold (typically 2–3). In this merged catalog, there are still duplicates from the different daughter catalogs attached to the different templates. Again, for detections separated by < 0.5 s, we keep only the detection with the highest average CC_{\max} and remove the others.

We perform a test on 1 day of data (14 September 2005) with both corrected and uncorrected optimal directions (Figure 3). For this test only, detections > 8 km away from their parent templates are included. The corrected catalog consists of 24% more detections (10,085 events) than the uncorrected (8152 events). The median of the average CC_{\max} values increases by 0.013 (Figure 3a) and the median of $R_{o/o}$ by 80% (Figure 3b). We then set the cutoff $R_{o/o}$ for the corrected catalog to be 2.5, such that the number of detections for the two catalogs is nearly the same ($R_{o/o}$ is not a useful quality control measure for the uncorrected catalog when splitting is significant). Figures 3c and 3d show the comparison between the uncorrected catalog and the corrected with the $R_{o/o}$ threshold. Instead of locations, time offsets between LZB and TWKB are plotted as a

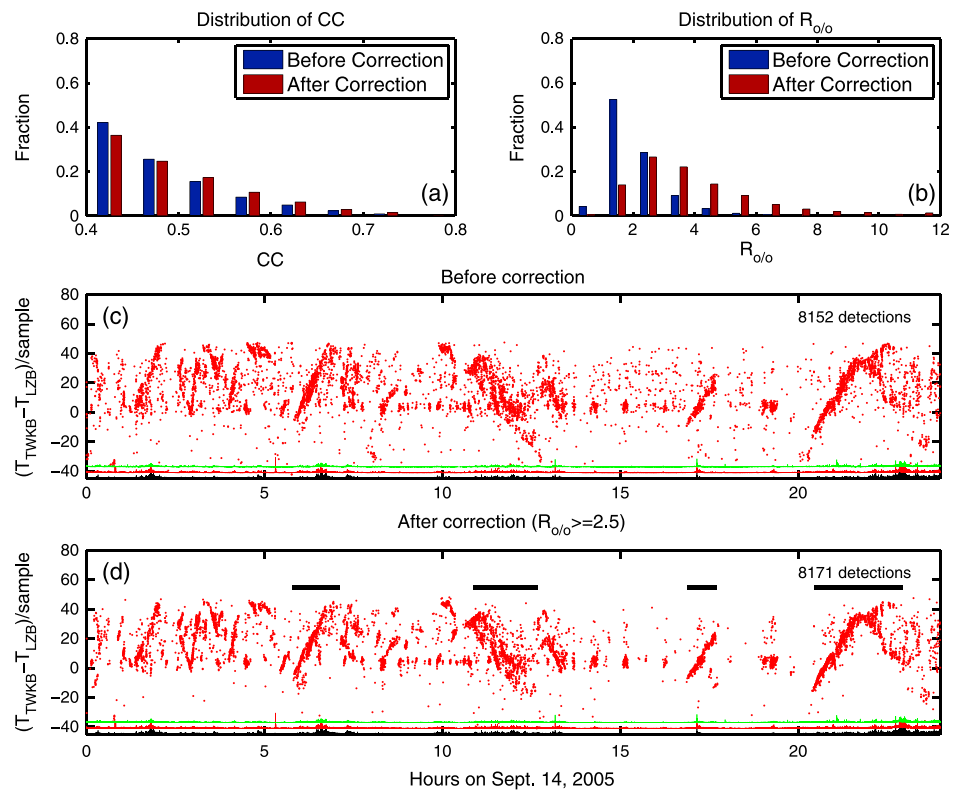


Figure 3. Comparison between tremor catalogs using the split-corrected polarization angles and the uncorrected. One day of data is used (14 September 2005). (a) Distribution of average CC_{max} before (blue bars) and after (red) correction. The median CC_{max} value increases by 0.013 after correction. (b) Distribution of $R_{o/o}$ before (blue bars) and after (red) correction. The median $R_{o/o}$ increases by 80% after correction. (c) Time offsets between LZB and TWKB for 8152 detections before correction as a function of time. (d) Time offsets between LZB and TWKB for detections after correction as a function of time. There are 8171 detections remaining after imposing a $R_{o/o}$ cutoff of 2.5. Traces at bottom of Figures 3c and 3d are the envelope of the seismograms at stations LZB (black), TWKB (red), and MGCB (green), showing the amplitudes of the tremor signal. Black bars in Figure 3d show times of the four RTMs in Figures 8a, 8b, 7c, and 8c.

function of time. Numerous bursts of rapid tremor migrations (RTMs) are visible. We observe that outliers that are likely to be caused by either bad correlation of a real signal (e.g., cycle skipping) or spurious correlation of noise are substantially reduced after applying the splitting correction and that after correction the RTMs appear sharper.

3. Results

3.1. Relative Location Errors Using Short Windows

We apply this short-window method to continuous seismic recordings during the three ETS episodes from 2003 to 2005. The detection thresholds are as in section 2.3 with the exception of the $R_{o/o}$ cutoff being 3. Detections more than 8 km away from their parent template are not included. We obtain 21,051 four second detections for 2005 (8 days), 15,118 for 2004 (10 days), and 13,640 for 2003 (8 days). Tremor locations as a function of time from the 2005 catalog are shown in Figures 4 and 5, and those from the 2003 and 2004 catalogs are illustrated in Figures S9–S12. Figures 6–10 show several selected RTMs. We consider two sources of relative location error that can affect these catalogs: spatially varying splitting corrections, and noise in the cross-correlation measurement. We introduce three different ways to quantify the relative location error empirically:

1. We assume that the smallest spatial extent of tremor migration fronts that can be resolved defines the relative location error. For many small-scale migrations such as those shown in Figures 6a, 6c, 6d, and 7d, it appears that the spatial scatter is about 1 km in the dip direction ($S60^{\circ}W-N60^{\circ}E$). This can be seen more clearly in Figures 11a–11d. This corresponds to a relative location error upper bound of ± 0.5 km in this direction. From our locations, we find that this error is roughly equivalent to an error of ± 1 sample for the

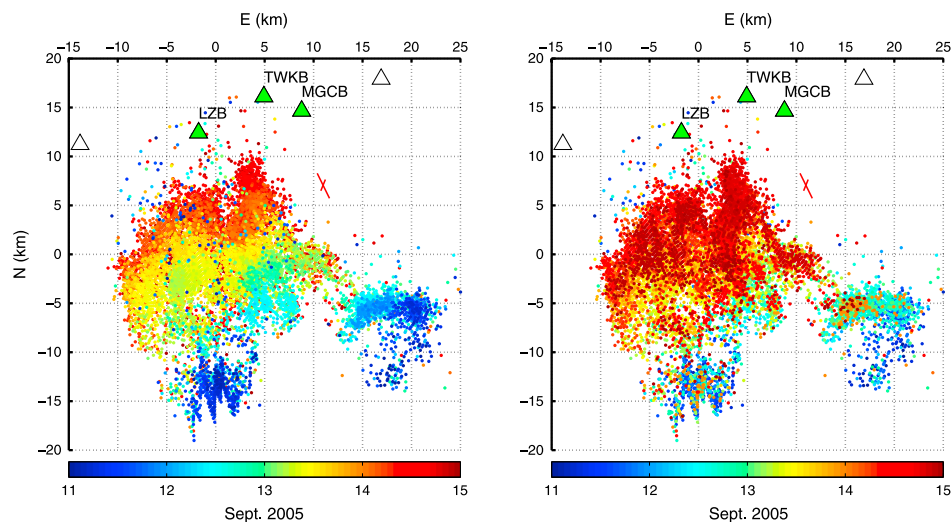


Figure 4. Locations of 16814 four second detections (colored circles progressing from blue to red) from 11 to 14 September 2005. (left) The earlier detections on top of the later ones. (right) Later on top of earlier. Triangles are stations and the LZB trio is colored green. The red cross indicates the change in location resulting from a ± 1 sample deviation in the time offsets for a representative template.

time offset between LZB and TWKB. Because of the station distribution within the LZB trio, the along-strike resolution is poorer. If we assume that a ± 1 sample error is also appropriate for the time offset between MGCB and TWKB, then the relative location error in the strike direction is $\leq \pm 1.5$ km. A few migrations with a spatial scatter of 2–3 km along strike, such as those shown in Figure S5, also validate this estimation. In Figures 4 and 6–10, the result of a ± 1 sample deviation from the time offsets for a representative template is shown by a red cross, as an estimate of the relative location error. The two red lines marking the cross are oblique to each other due to the station distribution within the LZB trio. Assuming a Gaussian distribution for the errors in the two independent time offsets, we find that the orientation of the major axis of the resulting error ellipse is very close to the long axis of the red crosses shown in Figures 4 and 6–10. Since we focus on a region only about 30 km across, the length and obliqueness of the red crosses do not vary much within the study region (they are shown for all 11 templates in Figure S6).

2. We attempt to search for a fourth arrival at nearby stations by comparing seismograms at the LZB trio with those at stations KLNB and TSJB (see supporting information for more details). For those with at least one additional arrival (about 50% of the total catalog), the time offsets between KLNB or TSJB and TWKB vary smoothly in space (Figure S7), and location differences within a region much smaller than 1 km can be

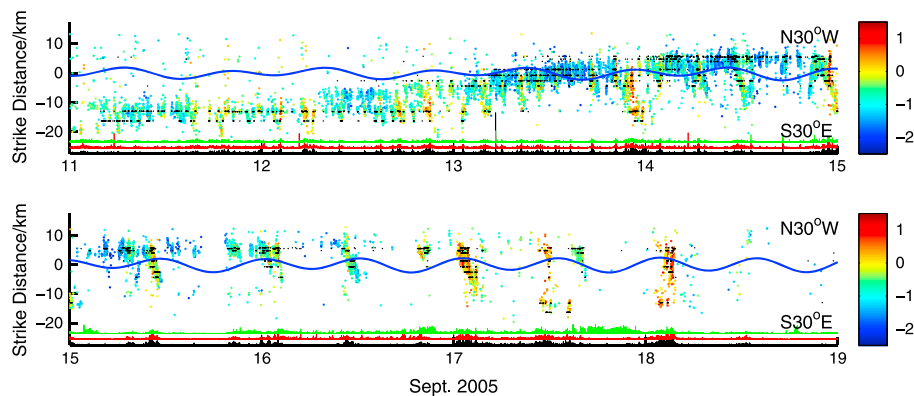


Figure 5. Along-strike ($N30^\circ W$) locations as a function of time for 4 s detections from 11 to 18 September 2005, color-coded by \log_{10} of the relative LFE radiated energy as defined in the text. Black dots show members of the 11 cross-time families indicated by black circles in Figure 1. Blue curves are computed thrust-promoting tidal shear stresses (in kPa). The main front of tremor migration propagates at a speed of 5 km/d along strike. Traces at bottom of Figures 5c and 5d are the envelopes of the seismograms at stations LZB (black), TWKB (red), and MGCB (green).

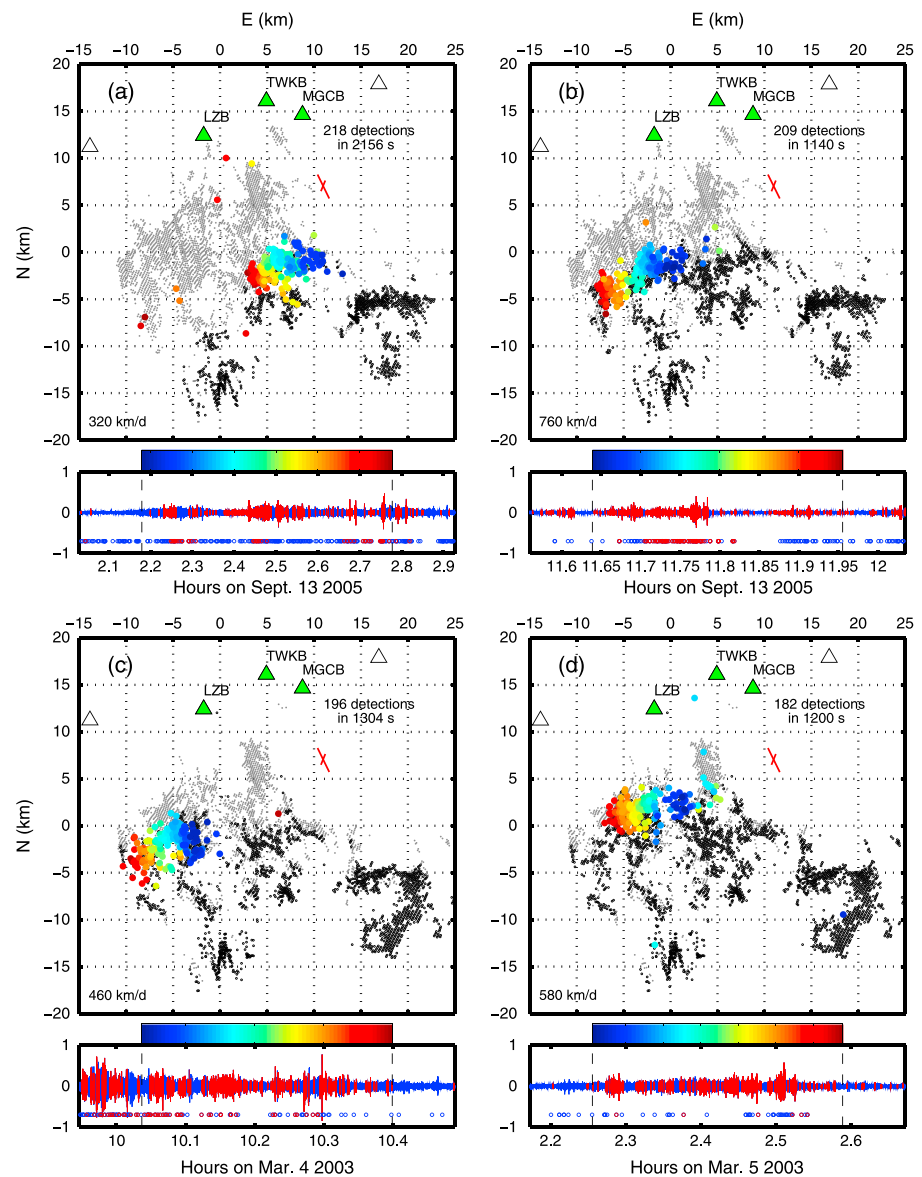


Figure 6. (a–d) Locations of 4 s detections (colored circles progressing from blue to red) of four tremor migrations during the 2003 and 2005 ETS episodes. Background dots (gray and black) indicate all 128-s detections during each episode; black symbols are those occurring up to and including the time window illustrated, delineating the approximate location of the main front. Triangles are stations and the LZB trio is colored green. Total number of 4 s detections in the time window are shown near the top right corner; on average there is one detection every 7 s. The approximate propagation speed is in the bottom left corner. The red cross indicates the change in location resulting from a ± 1 sample deviation in the time offsets for a representative template, as in Figure 4. (bottom) Blue trace is the east component of the velocity seismogram at station TWKB, and red sections are 4 s detections. Red circles show the occurrence times of members of the adopted 11 cross-time families of *Bostock et al.* [2012], and blue circles show their detections belonging to other families. Vertical dashed lines surround the time window shown in map view. Amplitude units are arbitrary but consistent for 2004 and 2005, and (separately) 2003.

resolved. This is consistent with the location error in the dip direction estimated above. We cannot constrain the location error in the strike direction using this method because KLN and TSJB are roughly colinear with the long dimension of the LZB trio.

3. In principle, duplicate detections associated with different templates should be at the same location as the optimal (highest CC_{max}) detection that is retained in the final catalog. We found that after the first step of removing duplicates in each catalog of daughter detections (see section 2.3), 90% of the duplicates associated with different templates are less than 2 km away from the corresponding optimal detections

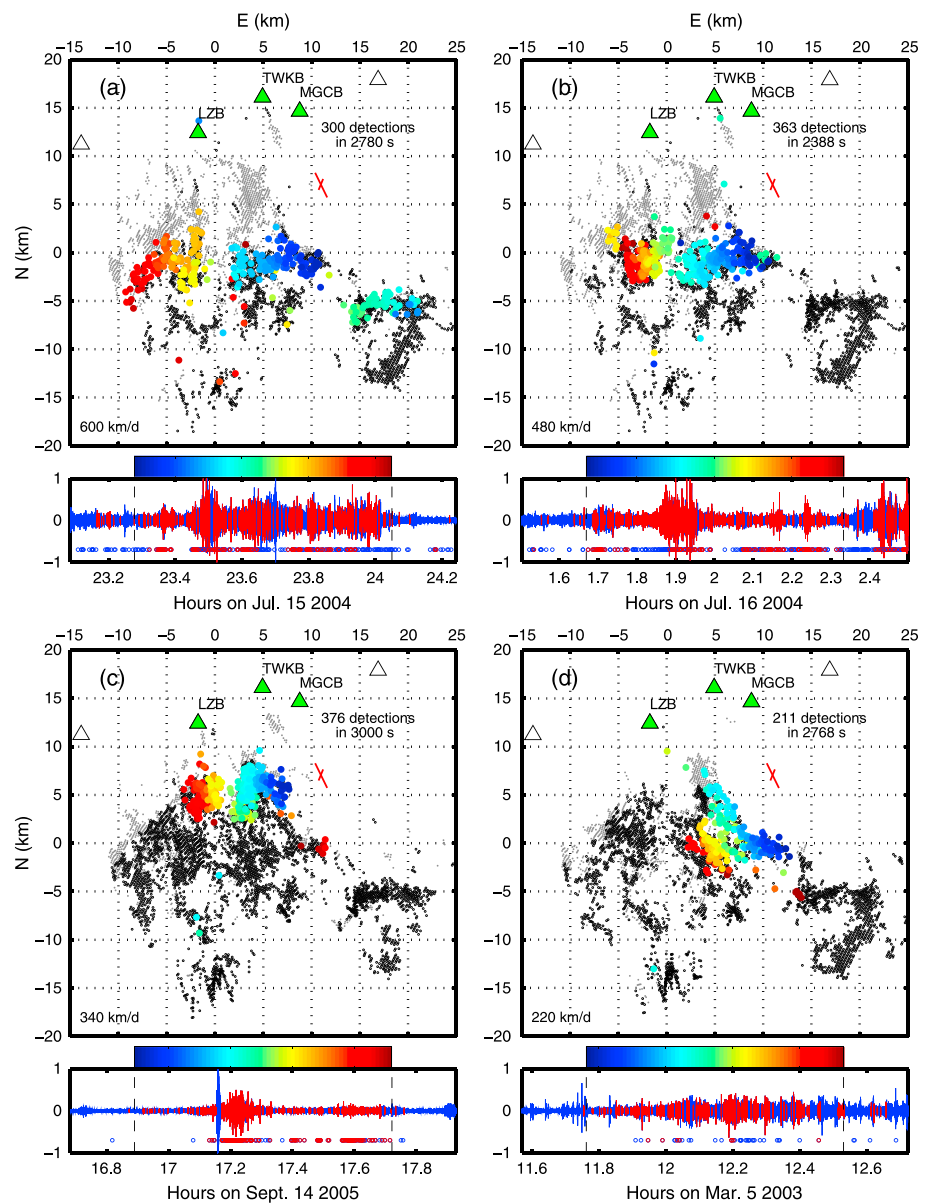


Figure 7. (a–d) Locations of 4 s detections within four tremor migrations during 2003–2005 ETS episodes. The migrations in Figures 7a–7c propagate along the main front from east to west, not along dip. Symbols are as in Figure 6. On average there is one detection every 8 s.

(Figure S8). We attribute most of the remainder to spurious correlation of noise. The fact that the CC_{max} values of the rejected duplicates are smaller than the corresponding optimal detections suggests that the location error for the duplicates is larger. Hence, 2 km should be viewed as the upper bound of the relative location error resulting from spatially variable splitting corrections.

3.2. General Pattern of Tremor Migrations

The main tremor front during the 2005 ETS episode is oriented roughly SW-NE and migrates along strike at a speed of 5 km/d (Figures 4 and 5), consistent with previous studies [e.g., *Wech et al., 2009; Kao et al., 2009*]. Figure 4 (left) shows the 4 s detections during the first 4 days of the 2005 catalog, while the main tremor front is within the study region, with earlier detections plotted on top of later ones. Figure 4 (right) shows the later on top of the earlier. Comparing the progression of colors in the two images, it can be seen that the leading edge of the main tremor front is much sharper than the trailing edge. On the other hand, during the 2003 and 2004 ETS episodes the main front is oriented roughly E-W (although it gradually progresses to the

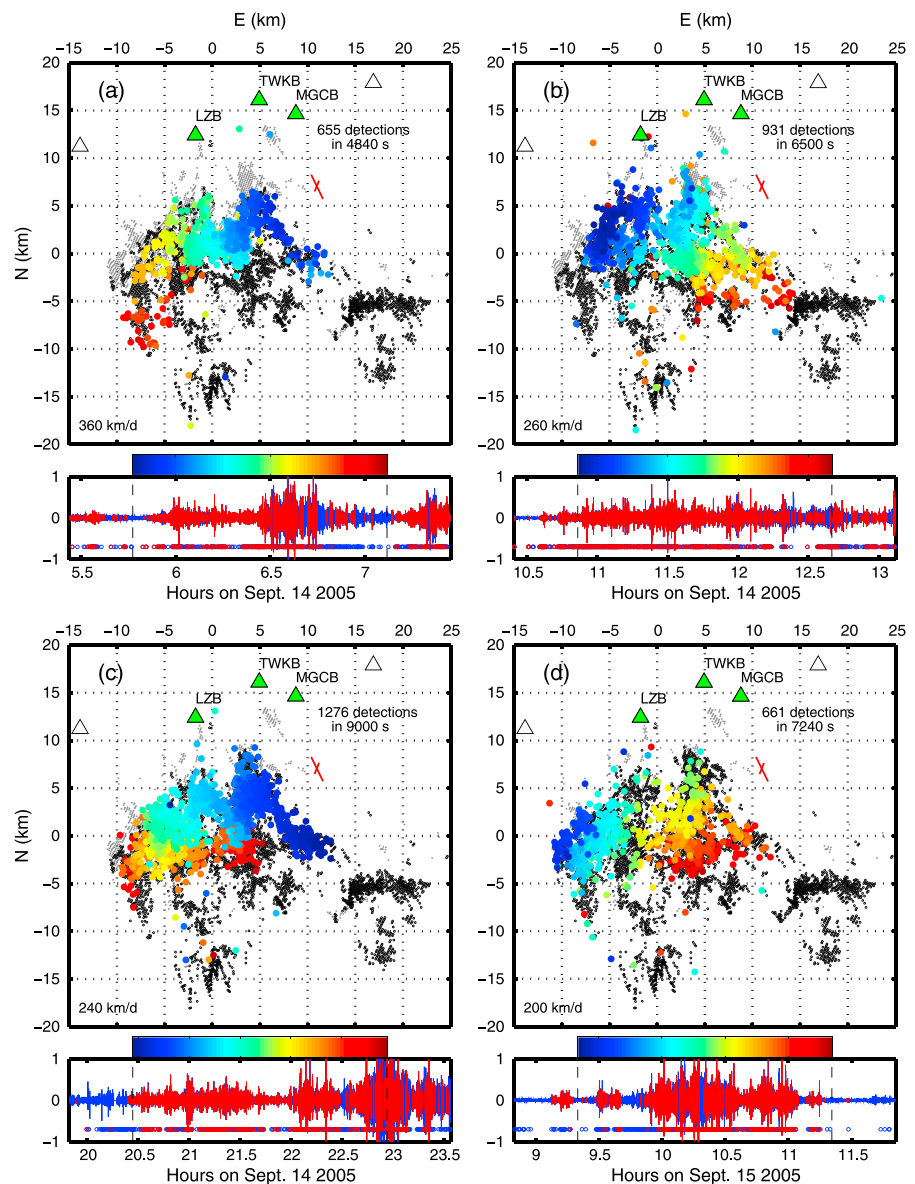


Figure 8. Locations of 4 s detections within four tremor migrations within about 30 h during the 2005 ETS episode (see also Figure 3d). Symbols are as in Figure 6. On average there is one detection every 8 s.

dip-parallel direction as it approaches the northwestern edge of the study region) and migrates at a slightly slower speed of 4 km/d (Figures S9 through S12). In Figure 5, symbol colors indicate relative radiated energy for each detection during the 2005 ETS episode, defined by integrating equation (1) over the most coherent 1 s interval within the 4 s window. The radiated energies span 4 orders of magnitude, and they are generally low near the main front, consistent with previous studies of more limited regions [Rubin and Armbruster, 2013; Sweet et al., 2012]. It is therefore possible that what we image as the main front actually lags the true slow slip front slightly, if the first tremor to occur in a region is below our detection threshold or is obscured by higher-amplitude tremor behind the front.

We note that the cross-time families from Bostock et al. [2012] show good consistency both spatially and temporally with the cross-station tremor locations (Figures 5, S10, and S12), with the latter showing more detailed migration patterns. Numerous RTM fronts propagate at speeds tens to hundreds of times faster than the main front. We identify very different styles of RTMs depending on the proximity to the main tremor front:

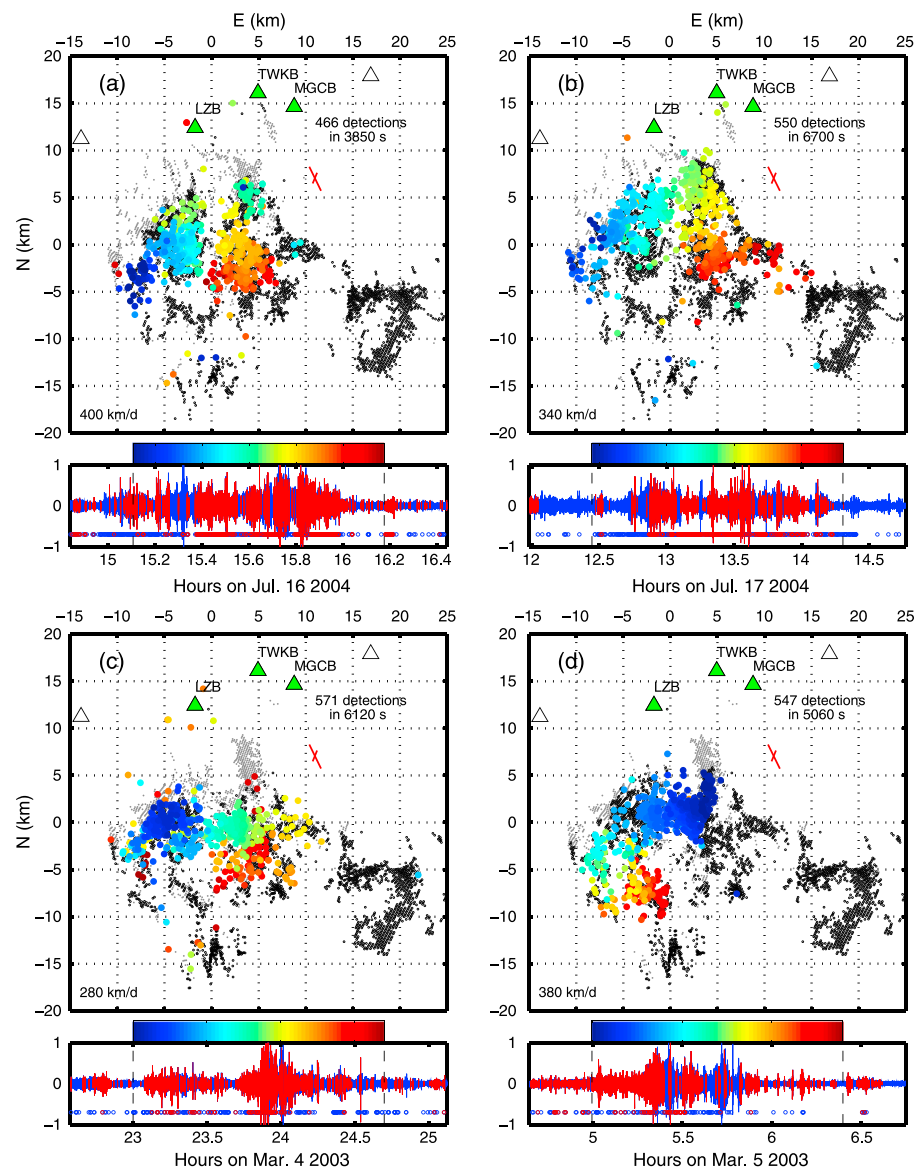


Figure 9. Locations of 4 s detections within four tremor migrations during 2003–2004 ETS episodes. These RTMs initially propagate along the main front and evolve into back-propagating fronts. Symbols are as in Figure 6. On average there is one detection every 10 s.

1. In the vicinity of the main front, there are numerous RTMs with recurrence intervals too short to be tidally driven. Most of these migrations propagate along the main front, either parallel to dip or in the EW direction, depending upon the orientation of that front (e.g., Figures 6 and 7). The widths of these secondary fronts in the propagation direction are about 1–3 km. The propagation speeds are in the range of 300–1000 km/d, comparable to the speeds of the slip-parallel tremor streaks described by *Ghosh et al.* [2010].
2. As the main front progressively moves out of the study region, the occurrences of secondary migrations behind the main front become more intermittent and are well correlated with peaks of tidal shear stresses computed for the center of the study region using the code of *Hawthorne and Rubin* [2010] (Figures 5, S10, and S12). This behavior indicates tidal modulation in this stage, and it persists through all 3 years, consistent with the results of *Thomas et al.* [2013] for more recent ETS episodes. Propagation velocities are in the range of 80–300 km/d, about the same as for the RTRs identified by *Houston et al.* [2011]. Front widths of the RTRs in their propagation direction appear to be larger than they were closer to the main front, about 4–6 km. Although the relative location error is larger in the strike direction, this difference appears to be too large to be accounted for by location error alone.

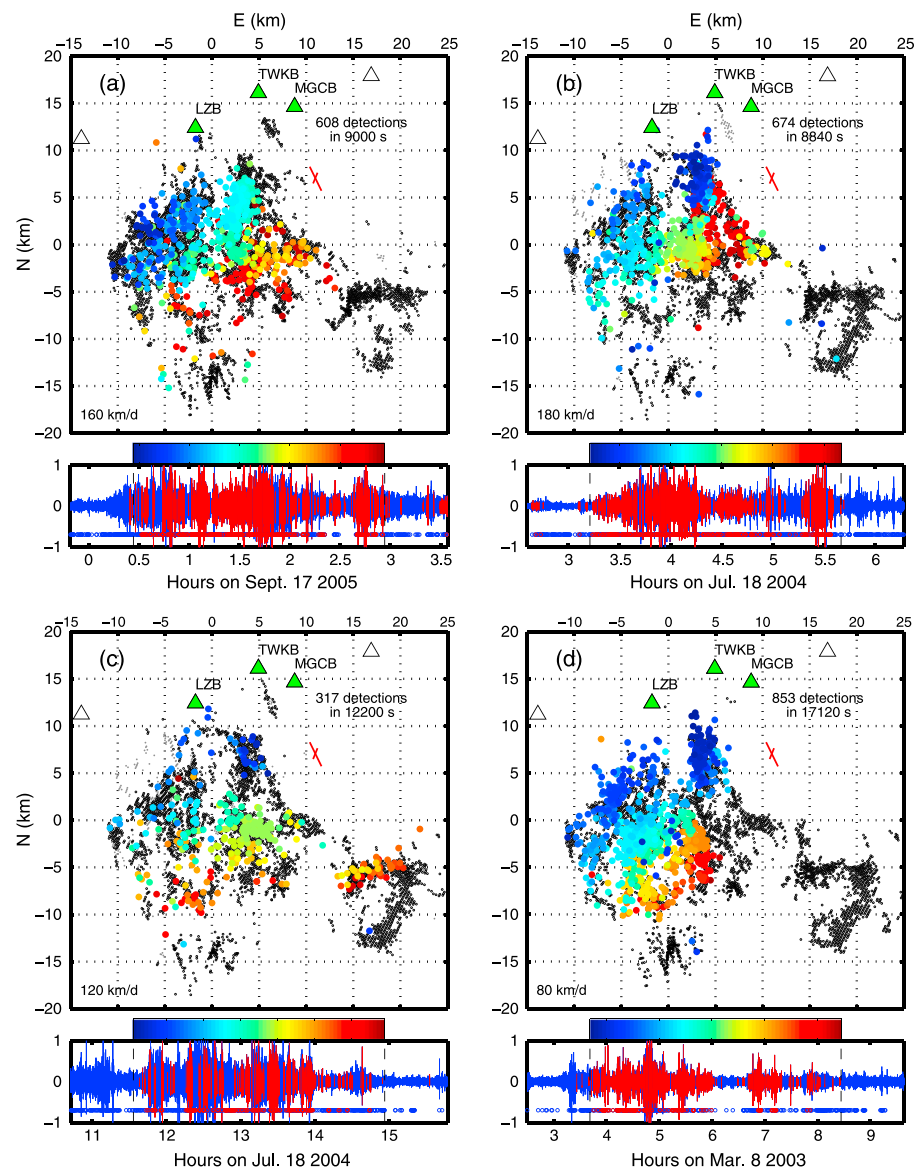


Figure 10. Locations of 4 s detections within four RTRs and quasi-RTRs during 2003–2005 ETS episodes. Symbols are as in Figure 6. On average there is one detection every 20 s.

3.3. Selected RTMs and Implications for Slow Slip Fronts

In this section we select a few RTMs during the three ETS episodes to illustrate the behaviors of slow slip fronts (Figures 6–10). Colored circles are short-window detections, progressing from blue to red in time. Background gray dots are all the long-window detections during each episode, a proxy for the regions capable of producing tremor. The current location of the main front can be inferred from long-window detections occurring up to and including the time window of the RTM illustrated, shown as black dots. Since long windows are less susceptible to cycle skipping and spurious correlation of noise than short windows, we find that they are preferable for delineating the main front. Figures 6 (bottom)–10 (bottom) show (in blue) the east component of the seismograms at station TWKB, with (in red) the 4 s windows with detections. For comparison, the blue circles below the seismograms show all the detection occurrence times from *Bostock et al.* [2012], including those from templates outside our study region and red circles are detections within the 11 cross-time families used as our parent templates.

Figure 6 shows several RTMs propagating along dip at the main front during the first stage of activity. Along-dip propagation over a somewhat larger length scale beneath the Olympic Peninsula was reported by

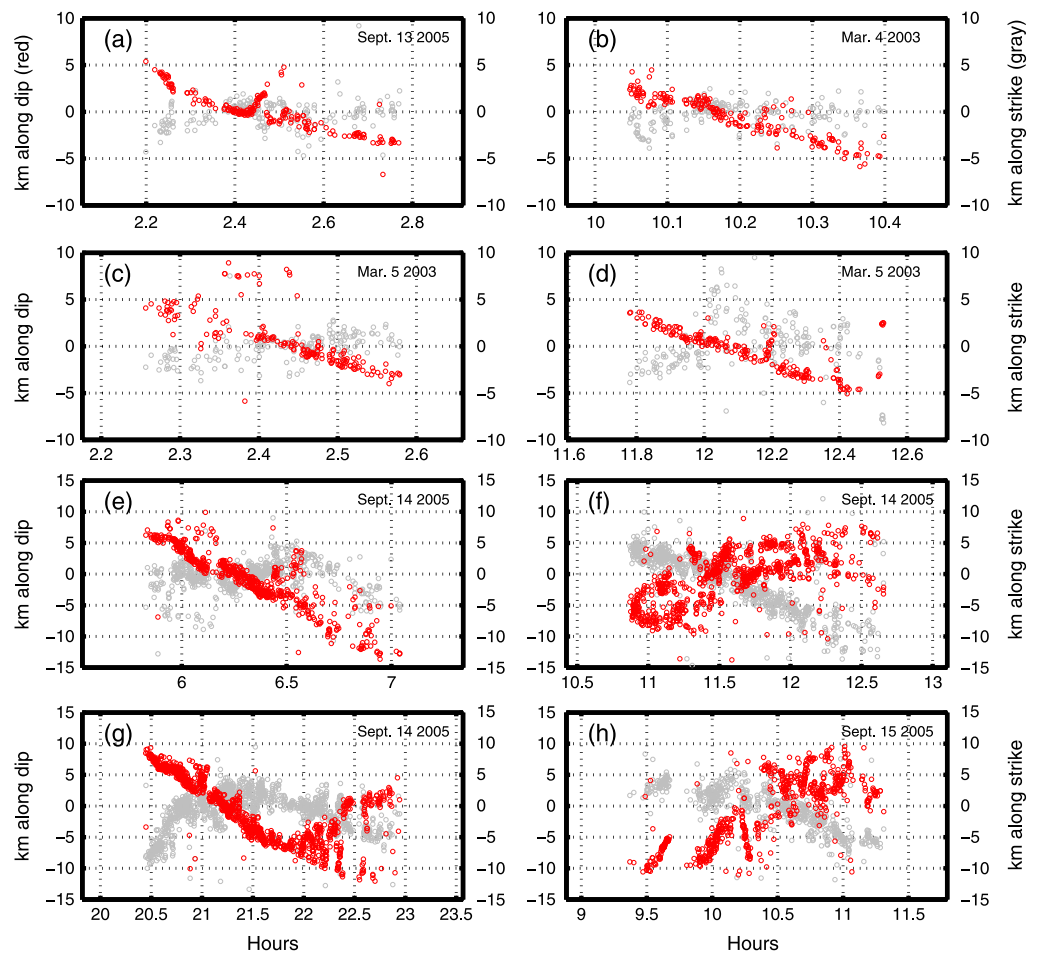


Figure 11. Along-strike (gray dots; N30°W is positive) and along-dip (red dots; downdip is positive) locations as a function of time for the 8 RTMs in Figures 6a, 6c, 6d, 7d, and 8. The strike direction is defined as N30°W.

Ghosh *et al.* [2010]. However, we also observe a relatively wide range of propagation azimuths of the RTMs (Figure S13), including those propagating neither along dip nor along strike, but in the EW direction (e.g., Figures 7a–7c). We interpret these to be RTMs propagating parallel to the current main front, which is not necessarily oriented in the dip direction and is sometimes curved. This interpretation is consistent with the observation that many EW-propagating RTMs occurred in 2003 and 2004, when the main front was for the most part oriented generally E-W rather than parallel to dip or slip (Figures S9 and S11). We quantify the tendency for RTMs to propagate parallel to the local main front in Figure S13. As an aside, we note that the source region hosting the westward migration shown in Figure 7c also hosted an along-dip migration in 2005 and a small-scale reversal in 2003 (Figures S14a and S14b). This further supports the contention that the propagation direction of RTMs at a given location is not solely a function of the local fault fabric.

In Figure 6 the apparent width of the tremor fronts in the propagation direction, which is the better resolved direction given the station locations of the LZB trio, is generally 1–2 km. The apparent width in the orthogonal direction is greater, but this could be due to the larger along-strike location error; as with the along-dip migrations near the main front observed by Rubin and Armbruster [2013], the front width orthogonal to the propagation direction is not resolved and could be quite small. Thus, the rapid propagation speed of these RTMs could be interpreted as an “apparent” velocity due to the main front moving progressively across an array of tremor sources. As originally proposed [e.g., Ando *et al.*, 2010; Gershenson *et al.*, 2011], it was suggested that there was an anisotropic distribution of these tremor sources on the fault surface, owing to the tendency for along-dip propagation of most known RTMs. However, the same rapid propagation along a slow slip front could conceivably occur in any orientation in the absence of an anisotropic fabric. Figure 7d illustrates the less common case where the migration seems to occur behind the main front. The front width orthogonal to

the propagation direction is larger than those in Figure 6, about 3–5 km, and larger than the inferred location error, while the propagation speed is smaller.

Most of the migrations imaged by *Rubin and Armbruster* [2013] occurred near the main front and propagated back along strike, not parallel to dip, and extended for only a few kilometers. We also see many localized “bursts” of tremor activity only a few kilometers across in our LZB catalog. These almost invariably occur at the main tremor front, and several of them may occur apparently independently within a time period of tens of minutes to an hour (Figures S14c and S14d). It is possible that some of these also represent back-propagating fronts of the size seen by *Rubin and Armbruster* [2013], but because of our poorer resolution in the strike direction, we would be unlikely to resolve such migrations.

During the 2005 ETS episode, we observe four larger-scale RTMs occupying roughly the same source area while the main front is still within the study region (Figure 8). The along-strike and along-dip locations as a function of time are shown in Figures 11e–11h. The propagation velocities from one to the next appear to decrease with time while the recurrence interval increases from 3 to 10 h. Except for the first example, these RTMs seem to be consistent with tidal modulation (Figure 5). Two of these migrations (Figures 8a and 8c) spend much of their time propagating along dip; the front lengths perpendicular to the migration direction for these RTMs are larger than 5 km (Figures 11e and 11g). The fact that our method is capable of resolving smaller along-strike extents in this region (e.g., Figures 6, 7, and S5) suggests that this elongation is not due to location error. This elongation is also supported by the locations of contemporaneous detections within the cross-time families of *Bostock et al.* [2012]. This observation is inconsistent with the interpretation that the large propagation speed of these along-dip migrations is an apparent velocity caused by the slow slip front intersecting a line of tremor sources [*Ando et al.*, 2010; *Ghosh et al.*, 2010].

We note that the migration shown in Figure 8c is actually the start of one of the 2005 RTRs identified by *Houston et al.* [2011]. In fact, our locations (see also Figure 11g) show that it originates behind the main front and first moves toward the main front, to the northwest. It then propagates generally updip along the main front, but in a somewhat zigzag fashion, and ends in a bilateral front, with one of its branches propagating back into the region that previously ruptured. This back-propagating branch becomes more diffuse subsequently as it evolves into an RTR propagating to the southeast (Figures S15a and S15b). Another reversal also seems to propagate in a complex fashion about 24 h earlier, near the end of 13 September 2005 (Figure 5). It begins with several migrations near the main front within a few hours, followed by a diffuse back-propagating front with high tremor amplitudes while many tremor sources near the main front remain active (Figures S15c and S15d).

The two migrations shown in Figures 8b and 8d appear more similar to RTRs than those in Figures 8a and 8c. They originate near the main front, and the azimuths of the propagating fronts progress from roughly along dip to E-W. In fact, Figure 11h shows that the starting phase of the second RTR is composed of three migrations moving roughly along dip, with the first two propagating downdip and the third updip, each slightly farther from the main front than the previous (blue to green colors in Figure 8d). Occasionally, we observe along-dip migrations in this same region during other RTRs, which might indicate the existence of anisotropic fabric on the fault surface. But these generally occurred after the main front moved beyond the study region. Considering that anisotropic fabric does not seem to be capable of altering the orientation of the main front (e.g., Figure 7) and that many RTMs propagate along the main front regardless of its orientation, we argue that the main front, rather than an anisotropic fabric on the fault, controls the migration patterns of RTMs occurring in its vicinity.

We also observe several migrations with a relatively complex propagation pattern (Figure 9), in some ways similar to those shown in Figure 8 and S15. The first half of these RTMs is reminiscent of small-scale RTMs close to the main front, in that they propagate parallel to the main front. The migrating fronts then change their propagation direction abruptly and become more reversal-like. One might argue that, instead of being true reversals, the two migrations in Figures 9b and 9d follow a highly curved main front. For Figure 9b we find this unlikely, since tremor locations downdip of our study region using the PGC-SSIB-SILB station trio [*Armbruster et al.*, 2014] seem not to support a main front that deviates so significantly from linearity (Figure S16). For the last half of the migration in Figure 9d, we are unable to constrain the shape of the main front due to the drastically decreased tremor density further updip. These RTMs with an abrupt change of their propagation directions are most often observed during the transition between the two styles of behavior described in section 3.2, and it suggests that at least some RTRs start by propagating along the main front.

As the main front gradually moves out of the study region, the area of the regions participating in the RTMs becomes larger, while the RTMs become more intermittent and more closely tied to favorable tidal shear stresses. Several examples are shown in Figure 10. The later portions of those in Figures 10a and 10c span a few large “gaps” where the tremor density is low, suggesting that these large-scale secondary fronts are roughly continuous in space despite the fact that the energetic tremor source regions are not. The RTM in Figure 10b appears to nucleate near the main front, propagate back, and subsequently evolve into an along-dip migration behind the main front. This highlights the fact that many RTMs and quasi-RTRs show complex migration patterns that are not well-characterized by time-distance plots that show only a single spatial coordinate. The migration pattern of the RTR shown in Figure 10d is relatively simple, although it propagates at a speed of 80 km/d, which is about a factor of 2–3 slower than the RTRs identified by *Houston et al.* [2011] and *Thomas et al.* [2013].

4. Conclusions

We have developed a cross-station method that correlates seismograms from the same time window at stations separated by 5–15 km, after rotating the horizontal components into the shear wave polarization direction. We obtain these polarization directions after correcting for shear wave splitting using 11 stacked templates from *Bostock et al.* [2012]. This significantly increases the number of detections and the resulting location accuracy. The ratio of the energy of the optimal component to that of the orthogonal is adopted as an additional quality control measure to weed out false detections. We estimate the upper bound of relative location error to be <2 km for short-window detections, with along-dip error significantly less than along strike.

Near the main front, we observe many small-scale RTMs propagating parallel to the main slow front of tremor migration, which is not necessarily in the dip direction and is sometimes curved. In particular, while the main front is oriented roughly parallel to dip during the 2005 ETS event, for the 2003 and 2004 events it is oriented roughly E-W. These observations suggest that although an anisotropic fabric may exist on the fault, the dominant influence on the migration pattern of secondary fronts in the vicinity of the main front comes from the orientation of that front and not the anisotropic fabric. Evidently, any anisotropic fabric is also insufficient to control the orientation of the main front. In addition, significant elongation along strike for several large-scale along-dip migrations and the occasional along-dip migration that occurs behind the main front argue against the interpretation that these RTMs are produced by the main slow slip front intersecting a linear slip-parallel structure on the fault. During this first stage of activity the recurrence intervals of RTMs is too short to be tidally modulated.

Farther behind the main front, most of the tremor activity occurs in the form of large-scale RTRs that are tidally modulated. The largest-scale RTRs that we image occur after the main front has propagated out of our study region to the NW, into an area where both our catalog and that of *Bostock et al.* [2012] lack tremor sources. These RTRs sometimes span portions of the fault with an apparently low density of tremor sources. This suggests that the secondary slip fronts that drive the RTRs are more continuous than the tremor sources that allow us to discern them. We note that when the main front has almost reached the northern edge of our study region, several RTMs that propagate along the main front eventually evolve into moderate-sized RTRs. Whether the slow slip underlying the largest RTRs we image also begins with propagation along the main front, we cannot say, owing to the lack of tremor sources immediately to the NW of our study region.

Acknowledgments

The seismic data used in this study were made available by the Canadian National Seismograph Network (<http://www.earthquakescanada.nrcan.gc.ca/stdon/index-eng.php>). We thank Jessica Hawthorne for providing the code for the tidal shear stress calculations. Two anonymous reviewers and the Associate Editor provided helpful reviews of this paper. Several figures were made using the GMT software of *Wessel and Smith* [1991]. This research was supported by NSF awards EAR-1214900 and EAR-1344948.

References

- Ando, R., R. Nakata, and T. Hori (2010), A slip pulse model with fault heterogeneity for low frequency earthquakes and tremor along plate interfaces, *Geophys. Res. Lett.*, *37*, L10310, doi:10.1029/2010GL043056.
- Armbruster, J. G., and W. Kim (2010), Coherent tremor in the Cascadia subduction zone. AGU, Fall Meeting 2010, abstract S11C-06.
- Armbruster, J. G., W. Kim, and A. M. Rubin (2014), Accurate tremor locations from coherent S and P waves, *J. Geophys. Res. Solid Earth*, *119*, 5000–5013, doi:10.1002/2014JB011133.
- Bartlow, N. M., S. Miyazaki, A. M. Bradley, and P. Segall (2011), Space-time correlation of slip and tremor during the 2009 Cascadia slow slip event, *Geophys. Res. Lett.*, *38*, L18309, doi:10.1029/2011GL048714.
- Beroza, G. C., and S. Ide (2011), Slow earthquakes and nonvolcanic tremor, *Annu. Rev. Earth Planet. Sci.*, *39*, 271–296.
- Bostock, M. G., and N. I. Christensen (2012), Split from slip and schist: Crustal anisotropy beneath northern Cascadia from non-volcanic tremor, *J. Geophys. Res.*, *117*, B08303, doi:10.1029/2011JB009095.
- Bostock, M. G., A. A. Royer, E. H. Hearn, and S. M. Peacock (2012), Low frequency earthquakes below southern Vancouver Island, *Geochem. Geophys. Geosyst.*, *13*, Q11007, doi:10.1029/2012GC004391.

- Bowman, J. R., and M. Ando (1987), Shear-wave splitting in the upper mantle wedge above the Tonga subduction zone, *Geophys. J. R. Astron. Soc.*, **88**, 25–41.
- Brown, J. R., G. C. Beroza, S. Ide, K. Ohta, D. R. Shelly, S. Y. Schwartz, W. Rabbel, M. Thorwart, and H. Kao (2009), Deep low-frequency earthquakes in tremor localize to the plate interface in multiple subduction zones, *Geophys. Res. Lett.*, **36**, L19306, doi:10.1029/2009GL040027.
- Crosson, R. S. (1976), Crustal structure modeling of earthquake data 2: Velocity structure of the Puget Sound region, Washington, *J. Geophys. Res.*, **81**, 3047–3054.
- Dragert, H., and K. Wang (2011), Temporal evolution of an episodic tremor and slip event along the northern Cascadia margin, *J. Geophys. Res.*, **116**, B12406, doi:10.1029/2011JB008609.
- Fukao, Y. (1984), Evidence from core-reflected shear waves for anisotropy in the Earth's mantle, *Nature*, **309**, 695–698.
- Gershenzon, N. I., G. Bambakidis, E. Hauser, A. Ghosh, and K. C. Creager (2011), Episodic tremors and slip in Cascadia in the framework of the Frenkel-Kontorova model, *Geophys. Res. Lett.*, **38**, L01309, doi:10.1029/2010GL045225.
- Ghosh, A., J. E. Vidale, J. R. Sweet, K. C. Creager, A. G. Wech, H. Houston, and E. E. Brodsky (2010), Rapid, continuous streaking of tremor in Cascadia, *Geochem. Geophys. Geosyst.*, **11**, Q12010, doi:10.1029/2010GC003305.
- Hawthorne, J. C., and A. M. Rubin (2010), Tidal modulation of slow slip in Cascadia, *J. Geophys. Res.*, **115**, B09406, doi:10.1029/2010JB007502.
- Hawthorne, J. C., and A. M. Rubin (2013), Short time scale correlation between slow slip and tremor in Cascadia, *J. Geophys. Res. Solid Earth*, **118**, 1316–1329, doi:10.1002/jgrb.50103.
- Houston, H., B. G. Delbridge, A. G. Wech, and K. C. Creager (2011), Rapid tremor reversals in Cascadia generated by a weakened plate interface, *Nat. Geosci.*, **4**(6), 404–409, doi:10.1038/ngeo1157.
- Ide, S., D. R. Shelly, and G. C. Beroza (2007), Mechanism of deep low frequency earthquakes: Further evidence that deep non-volcanic tremor is generated by shear slip on the plate interface, *Geophys. Res. Lett.*, **34**, L03308, doi:10.1029/2006GL028890.
- Ito, Y., K. Obara, K. Shiomi, S. Sekine, and H. Hirose (2007), Slow earthquakes coincident with episodic tremors and slow slip events, *Science*, **315**, 503–506.
- Kao, H., S.-J. Shan, H. Dragert, and G. Rogers (2009), Northern Cascadia episodic tremor and slip: A decade of tremor observations from 1997 to 2007, *J. Geophys. Res.*, **114**, B00A12, doi:10.1029/2008JB006046.
- Klein, F. W. (2002), User's Guide to HYPOINVERSE2000, a Fortran Program to solve for earthquake locations and magnitudes, *U.S. Geol. Surv. Open File Rep.*, **02–171**, pp. 1–123, U.S. Geol. Surv., Menlo Park, Calif.
- McCroary, P. A., J. L. Blair, D. H. Oppenheimer, and S. R. Walter (2004), Depth to the Juan de Fuca slab beneath the Cascadia subduction margin—A 3-D model for sorting earthquakes, *U.S. Geol. Surv. Tech. Rep.*, **91**, pp. 1–13, U.S. Geol. Surv., Menlo Park, Calif.
- Matharu, G., M. G. Bostock, N. I. Christensen, and J. Tromp (2014), Crustal anisotropy in a subduction zone forearc: Northern Cascadia, *J. Geophys. Res. Solid Earth*, **119**, 7058–7078, doi:10.1002/2014JB011321.
- Nicholson, T., M. G. Bostock, and J. F. Cassidy (2005), New constraints on subduction zone structure in northern Cascadia, *Geophys. J. Int.*, **161**, 191–205, doi:10.1111/j.1365-246X.2005.02605.x.
- Obara, K. (2012), Depth-dependent mode of tremor migration beneath Kii Peninsula, Nankai subduction zone, *Geophys. Res. Lett.*, **39**, L10308, doi:10.1029/2012GL051420.
- Obara, K., H. Hirose, F. Yamamizu, and K. Kasahara (2004), Episodic slow slip events accompanied by non-volcanic tremors in southwest Japan subduction zone, *Geophys. Res. Lett.*, **31**, L23602, doi:10.1029/2004GL020848.
- Rogers, G., and H. Dragert (2003), Episodic tremor and slip on the Cascadia subduction zone: The chatter of silent slip, *Science*, **300**(5627), 1942–1943, doi:10.1126/science.1084783.
- Royer, A. A., and M. G. Bostock (2013), A comparative study of low frequency earthquake templates in northern Cascadia, *Earth Planet. Sci. Lett.*, **247**–256, doi:10.1016/j.epsl.2013.08.040.
- Rubin, A. M., and J. G. Armbruster (2013), Imaging slow slip fronts in Cascadia with high precision cross-station tremor locations, *Geochem. Geophys. Geosyst.*, **14**, 5371–5392, doi:10.1002/2013GC005031.
- Shelly, D. R. (2010), Migrating tremors illuminate complex deformation beneath the seismogenic San Andreas fault, *Nature*, **463**(7281), 648–652.
- Shelly, D. R., G. C. Beroza, and S. Ide (2007a), Non-volcanic tremor and low-frequency earthquake swarms, *Nature*, **446**, 305–307, doi:10.1038/nature05666.
- Shelly, D. R., G. C. Beroza, and S. Ide (2007b), The complex evolution of transient slip derived from precise tremor locations in western Shikoku, Japan, *Geochem. Geophys. Geosyst.*, **8**, Q10014, doi:10.1029/2007GC001640.
- Silver, P. G., and W. W. Chan (1991), Shear wave splitting and subcontinental mantle deformation, *J. Geophys. Res.*, **96**, 16,429–16,454.
- Sweet, J. R., K. C. Creager, T. Thomas, J. E. Vidale, and H. Houston (2012), Unlocking the secrets of slow slip on the plate interface using Cascadia LFEs, Abstract S431-04, presented at 2012 Fall Meeting, AGU, San Francisco, Calif.
- Szeliga, W., T. Melbourne, M. Santillan, and M. Miller (2008), GPS constraints on 34 slow slip events within the Cascadia subduction zone, 1997–2005, *J. Geophys. Res.*, **113**, B04404, doi:10.1029/2007JB004948.
- Teanby, N. A., J.-M. Kendall, and M. van der Baan (2004), Automation of shear-wave splitting measurements using cluster analysis, *Bull. Seismol. Soc. Am.*, **94**, 453–463.
- Thomas, T. W., J. E. Vidale, H. Houston, K. C. Creager, J. R. Sweet, and A. Ghosh (2013), Evidence for tidal triggering of high-amplitude rapid tremor reversals and tremor streaks in northern Cascadia, *Geophys. Res. Lett.*, **40**, 4254–4259, doi:10.1002/grl.50832.
- Wech, A. G., and K. C. Creager (2007), Cascadia tremor polarization evidence for plate interface slip, *Geophys. Res. Lett.*, **34**, L22306, doi:10.1029/2007GL031167.
- Wech, A. G., K. C. Creager, and T. I. Melbourne (2009), Seismic and geodetic constraints on Cascadia slow slip, *J. Geophys. Res.*, **114**, B10316, doi:10.1029/2008JB006090.
- Wessel, P., and W. H. F. Smith (1991), Free software helps map and display data, *Eos Trans. AGU*, **72**, 441.